





# Investigating TeV Emissions from Simulated CTAO Data for the FSRQ 3C 279

REU Program at Columbia University - Nevis Labs

Salma Ibrahim<sup>1</sup>

<sup>1</sup>Columbia University

February 21, 2025

#### Abstract

Flat Spectrum Radio Quasars (FSRQs) are a subclass of Active Galactic Nuclei (AGN) characterized by extremely powerful emissions across the electromagnetic spectrum. However, gamma-ray detections of quasars in the TeV range remain a rarity as they are known to have highly variable emissions on timescales as small as a few minutes. The Cherenkov Telescope Array Observatory (CTAO) is expected to have record-high sensitivity observations in TeV ranges that will allow for a new and more comprehensive understanding of the most energetic AGN and their associated relativistic jets. This project utilizes simulated CTAO data for two FSRQs, 3C 279 and PKS 1510-089, to develop and test analysis pipelines using Gammapy, the core library for CTAO science tools which will serve as a primary open-source analysis software for future TeV gamma-ray astronomy.

## Contents

1	Introduction									
	1.1 Cosmic Rays	3								
	1.2 Gamma-ray Production Mechanisms: AGN	4								
	1.3 IACTs: CTAO	7								
<b>2</b>	Analysis	9								
	2.1 CTAO Science Data Challenge & Gammapy	9								
	2.2 Analysis Pipeline	9								
	2.2.1 Data Selection and Preprocessing	10								
	2.2.2 Background Estimation	11								
	2.2.3 Spectral Modeling and Fitting	11								
3	Results	12								
	3.1 3C 279	12								
	3.2 PKS 1510-089	13								
4	4 Summary and Conclusions									
5	6 Acknowledgments									
$\mathbf{A}$	A Appendix: Flux Point Tables									

#### 1 Introduction

Very high energy (VHE) gamma-ray observations offer indirect methods for studying the highest energy cosmic rays in our universe. Non-thermal processes occurring in extremely energetic astrophysical environments, such as active galactic nuclei and supernova remnants, produce VHE cosmic rays, which consist mainly of protons, along with gamma rays, and neutrinos. Of the three components, only gamma rays and neutrinos can be traced back to their original source since the charged protons and other atomic nuclei are deflected due to interactions with interstellar and intergalactic magnetic fields. Cosmic-ray particles can have near-light speed and energies exceeding 10<sup>20</sup> eV. Studying gamma rays in TeV ranges can allow for a more robust understanding of the cosmic-ray production mechanisms taking place in such high-energy sources.

Incident gamma rays on the Earth's atmosphere produce cascading particle air showers, which, in turn, result in the production of blue Cherenkov light. The use of this Cherenkov light to indirectly detect and reconstruct the properties of the primary gamma ray is called the Cherenkov technique. This indirect observation method is used by all ground-based gamma-ray telescopes, commonly known as Imaging Atmospheric Cherenkov Telescopes (IACTs). The newest addition to ground-based gamma-ray observation programs is the Cherenkov Telescope Array Observatory (CTAO). It will be the most powerful IACT ever and will have unprecedented sensitivity and sky coverage with its two sub-arrays: CTAO-North and CTAO-South. CTAO will provide insight into the highly energetic physical processes occurring in galactic and extra-galactic sources of TeV gamma rays. This will allow us to gain crucial insight into the origin of cosmic rays and the largest particle accelerators in the universe.

Nearly a third of all known TeV sources are active galactic nuclei (AGN) of the blazar class. Blazars are further subdivided into BL lacertae and flat-spectrum radio quasars (FSRQs) [1]. FSRQs are the most luminous blazars at GeV energies. However, they rarely emit detectable fluxes of TeV gamma rays, an event which typically only occurs during bright GeV flares. Gamma-ray emissions originate in the relativistic jets pointed outward from the two polar regions of AGN. TeV observations of AGN help us constrain models of particle acceleration and energy dissipation in blazar jets.

In this study, we analyzed simulated data from the second CTAO Science Data Challenge to investigate the TeV gamma-ray emission from two FSRQs: 3C 279 and PKS 1510-089. These sources are of interest to future observations and were selected due to their historical significance as bright FSRQs, and their inclusion in the CTAO dataset, providing an opportunity to explore the observatory's capabilities in detecting and characterizing FSRQs at TeV energies.

A primary objective of this study was to evaluate and refine gamma-ray data analysis techniques using Gammapy, a recently developed, open-source Python package designed for high-energy astrophysics. We implemented a comprehensive analysis pipeline that included event selection, background modeling, spectral fitting, and significance testing to characterize the TeV spectral properties of both sources. The results provide insights into the TeV emission mechanisms of FSRQs, aiding in our understanding of how relativistic jets produce high-energy radiation.

#### 1.1 Cosmic Rays

The study of VHE astronomy was originally motivated by the broader scientific pursuit of understanding the origin of cosmic rays, which were first discovered by Victor Hess in 1912 during his famous balloon experiments [2]. Hess conducted balloon flights carrying sensitive electrometers to measure ionization levels as a proxy for radiation intensity. By performing the experiment during a solar eclipse, he ruled out the possibility that the sun could be the primary source of the observed high-energy radiation. Hess concluded that a new type of high-energy radiation, originating from outer space, was responsible for the increased ionization at high altitudes—a groundbreaking discovery that earned him the 1936 Nobel Prize in Physics and laid the foundation for modern cosmic-ray and high-energy astrophysics.

Cosmic rays are now understood to be high-energy particles, primarily composed of protons ( $\sim 90\%$ ), helium nuclei ( $\sim 9\%$ ), and heavier nuclei ( $\sim 1\%$ ), with a small fraction of electrons and positrons [4]. These particles travel at near-light speeds and span an enormous range of energies, from  $10^9\,\mathrm{eV}$  (GeV) to beyond  $10^{20}\,\mathrm{eV}$  (EeV). The cosmic ray energy spectrum, shown in Fig. 1, has been shown to exhibit several distinct features: The knee ( $10^{15}\,\mathrm{eV}$ ), a change in the spectral slope, which is likely indicating the maximum energy achievable by supernova remnants; the ankle ( $10^{18}\,\mathrm{eV}$ ), or a flattening of the spectrum, likely due to the transition from galactic to extragalactic cosmic ray sources; and finally, the GZK cutoff ( $10^{19.5}\,\mathrm{eV}$ ), which is a suppression of the flux due to interactions with the cosmic microwave background.

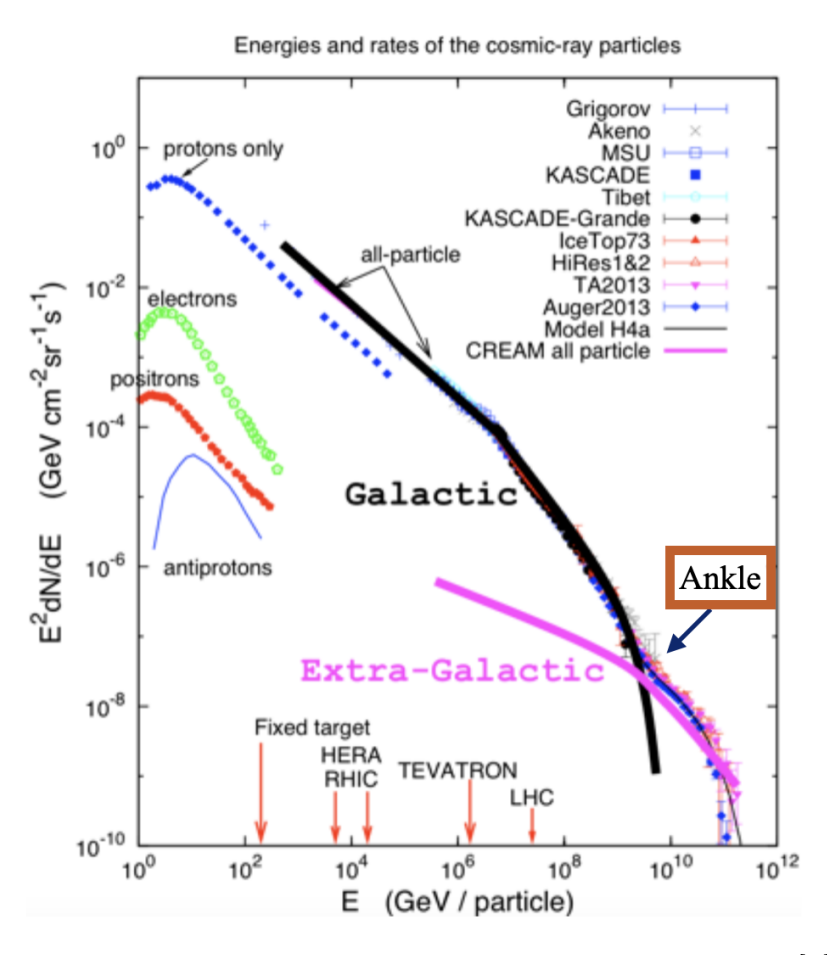


Figure 1: Cosmic ray intensity as a function of energy [3].

Despite over a century of research, the origin and acceleration mechanisms of these VHE cosmic rays remain largely unknown. Leading theories believe that extragalactic sources, such as AGN and gamma-ray bursts (GRBs), are the most likely candidates for producing the highest energy cosmic rays which lie beyond the ankle (  $10^{18} \,\mathrm{eV}$ ). AGN are powered by supermassive black holes, which launch relativistic jets capable of accelerating particles to extreme energies. GRBs, on the other hand, involve relativistic shock waves from massive stellar explosions, making them potential sources of ultra-high-energy cosmic rays.

However, a primary challenge in validating these sources is that charged cosmic rays are deflected by galactic and extragalactic magnetic fields, causing them to lose directional information. Consequently, they cannot be directly traced back to their sources. This has led to the emergence of *multi-messenger astronomy* where neutrinos and gamma rays are used as complementary probes. This is illustrated in Fig. 2. Unlike cosmic rays, magnetic fields do not deflect these neutral messengers, preserving the directional information and pointing directly to the cosmic accelerators.

The study of VHE gamma rays is directly linked to understanding cosmic rays, as gamma rays are typically secondary products of cosmic ray interactions. By investigating the gamma-ray e mission from powerful cosmic accelerators like AGN, we can gain crucial insights into the acceleration mechanisms of cosmic rays and the physical conditions in the relativistic jets which produce them.

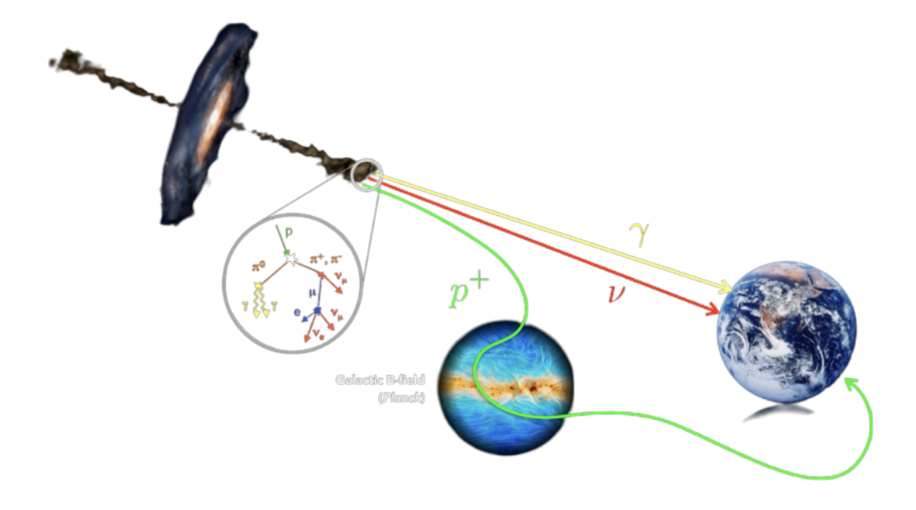


Figure 2: Illustration showing hadronic processes in jets of AGN. Multimessenger techniques are often used to explore AGN jets [5].

## 1.2 Gamma-ray Production Mechanisms: AGN

The catalog of known TeV sources currently consists of 308 total sources, 90 of which are AGNs. Given that approximately one-third of all known VHE gamma-ray sources are AGN, they are a crucial population of interest for understanding the most energetic astrophysical processes. Fig. 3 shows a skymap of know VHE sources. AGN are shown as red circles.

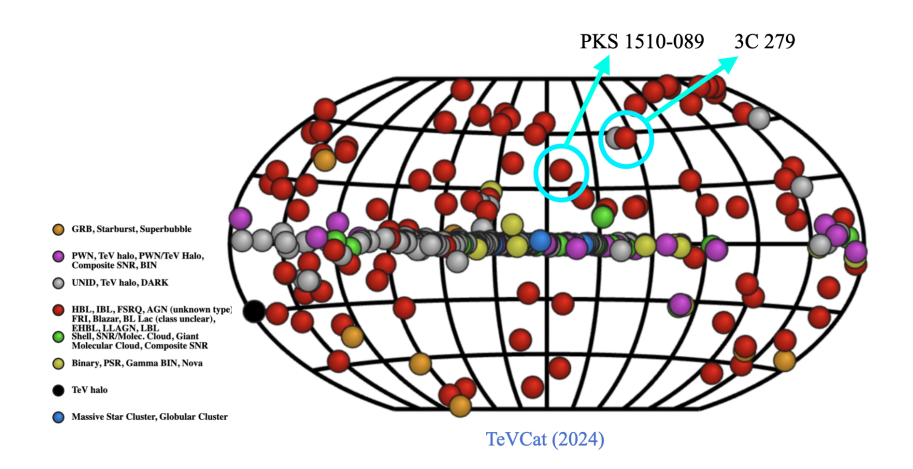


Figure 3: TeV gamma-ray sky map from TeVCat (2024), showing the distribution of known TeV sources, where AGN are represented in red. The locations of the FSRQs analyzed in this paper, PKS 1510-089 and 3C 279, are highlighted [6].

AGN are among the most powerful and luminous sources of radiation in the universe, capable of accelerating particles to ultra-relativistic speeds. They are powered by supermassive black holes with masses ranging from millions to billions of solar masses, surrounded by accretion disks of gas and dust, illustrated in Fig. 4. As matter spirals into the black hole, gravitational energy is converted into radiation, launching powerful relativistic jets that emit across the entire electromagnetic spectrum, including VHE gamma rays.

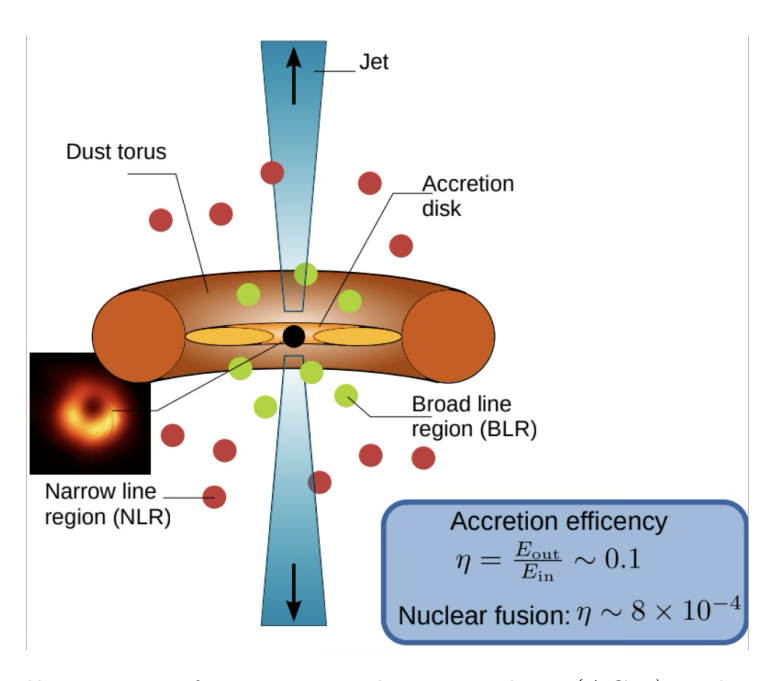


Figure 4: Schematic illustration of an active galactic nucleus (AGN) with a relativistic jet. The central supermassive black hole (SMBH) is surrounded by an accretion disk, which fuels the AGN's high-energy emissions [7].

AGN are classified based on the power and orientation of their jets relative to the observer's line of sight, as shown in Fig. 5. FSRQs are a subclass of blazars that are par-

ticularly interesting due to their powerful relativistic jets, which are directed toward our line of sight. This alignment produces beamed emission, and as a result, many blazars show superluminal motion in their jets and have a gamma-ray luminosity dominating their bolometric power [8]. In relativistic jet models, the broadband emission observed from blazars, spanning from radio to ultraviolet wavelengths, is primarily attributed to synchrotron radiation produced by high-energy electrons within the jet. These electrons are accelerated to ultra-relativistic speeds as they propagate along a highly collimated outflow, which is launched from the vicinity of a supermassive black hole (SMBH) actively accreting matter. The strong magnetic fields threading the jet cause these charged particles to spiral, emitting synchrotron radiation across a broad spectrum. This emission process accounts for the low-energy hump in the characteristic spectral energy distribution (SED) of blazars and serves as a key signature of particle acceleration and magnetic field interactions in the jet environment [9].

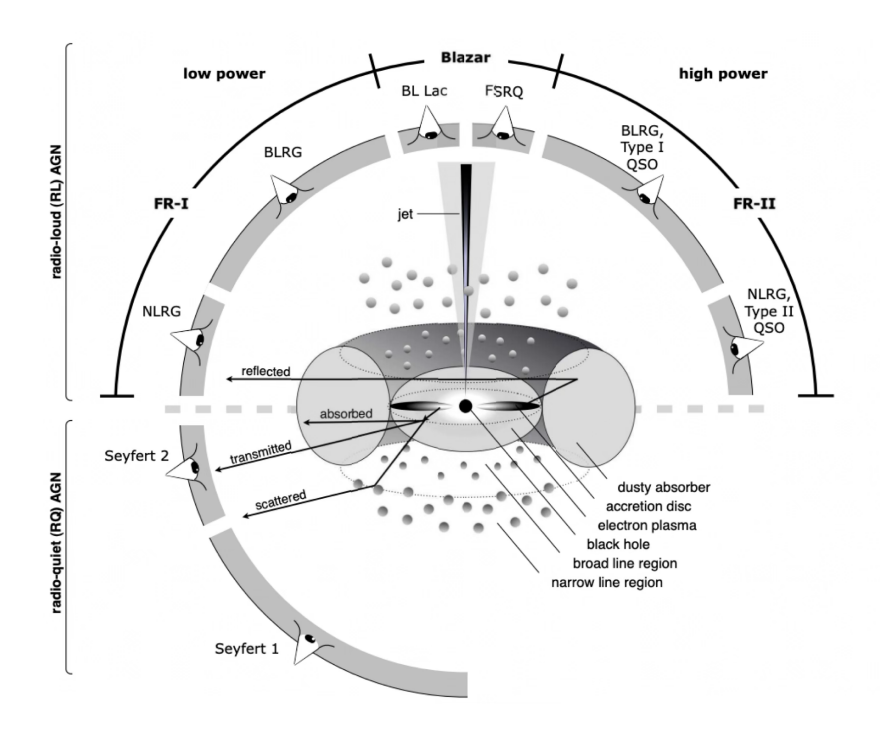


Figure 5: Schematic Diagram of the AGN phenomenon [10].

FSRQs are among the most luminous blazars at GeV energies, yet they rarely exhibit detectable TeV emissions. This makes their rare TeV flares invaluable opportunities to test theoretical models of high-energy radiation processes. It is likely that this challenge arises due to the effects of external radiation fields, which simultaneously enhance gamma-ray production at GeV energies and suppress emission at TeV energies. A major factor in this effect is the increased cooling of relativistic electrons due to *inverse Compton scattering*. The presence of intense photon fields from the broad line region (BLR) and the dusty torus enhances the efficiency of Compton cooling, causing high-energy electrons to lose energy more rapidly. As a result, fewer electrons reach the extreme energies required to produce TeV photons, leading to a steeper gamma-ray spectrum and a suppression of emission at the GeV cutoff [11]. Equation (1) demonstrates why external radiation fields in FSRQs shift the gamma-ray peak to GeV energies, as the external photon fields (UV from the BLR, IR from the torus) provide soft target photons for inverse Compton scattering:

$$E_{\gamma} = \frac{4}{3} \gamma^2 E_{\text{seed}} \tag{1}$$

Here  $E_{\gamma}$  is the energy of the upscattered gamma-ray photon,  $\gamma$  is the Lorentz factor of the relativistic electron, and  $E_{\text{seed}}$  is the energy of the seed photon from the BLR or torus.

Another critical factor limiting TeV emission from FSRQs is photon-photon pair production  $(\gamma \gamma \to e^+e^-)$ , which leads to significant absorption of high-energy gamma rays. When TeV photons interact with the dense UV and infrared photon fields of the BLR and dusty torus, they have a high probability of producing electron-positron pairs, effectively suppressing the TeV flux before it can escape the source. The optical depth for this process increases with energy, creating a characteristic spectral cutoff at TeV energies. Since the interaction probability depends on the energy of the incoming gamma-ray photon and the soft photon density, FSRQs with dense radiation fields experience stronger TeV suppression compared to BL Lac objects, which lack significant external photon fields. Consequently, detecting TeV emission from FSRQs is extremely rare, and such detections provide crucial information about the structure of AGN jets and the location of the gamma-ray emission region. If the gamma-ray production site lies within the BLR, the TeV flux is expected to be highly suppressed due to pair production. However, if the emission region is located beyond the BLR, where the photon density is lower, then more TeV gamma rays can escape. Observations of FSRQs at TeV energies help test these models by determining whether gamma-ray emission originates inside or outside the BLR. The observed TeV flux can, therefore, provide constraints on the size and location of the emission region and the level of external radiation fields.

#### 1.3 IACTs: CTAO

The Cherenkov Telescope Array Observatory (CTAO) represents the next generation of IACTs, designed to detect VHE gamma rays in the energy range from 20 GeV to 300 TeV [12]. Ten times more sensitive than existing IACTs such as VERITAS, H.E.S.S., and MAGIC, CTAO is set to revolutionize gamma-ray astronomy with its unparalleled sensitivity, wide energy coverage, and superior angular resolution, allowing for detailed studies of the most extreme astrophysical environments such as those occurring in FSRQs. CTAO will consist of an array of telescopes of different sizes and configurations. A cartoon of the array is shown in Fig. 6.

VHE gamma-ray photons are not directly detectable from Earth's surface [13]. They interact with atmospheric particles, initiating cascades of secondary particles through pair production and electromagnetic showers. When a high-energy gamma ray collides with a nucleus in the upper atmosphere, it produces an electron-positron pair, which subsequently undergoes bremsstrahlung, emitting additional high-energy photons. These secondary photons, in turn, create more electron-positron pairs, resulting in a rapidly developing particle cascade known as an extensive air shower. As these charged particles travel faster than the speed of light in the atmosphere, they emit Cherenkov radiation—a faint, bluish light that can be detected from the ground. This emission lasts only a few nanoseconds, requiring highly sensitive, fast-response telescopes to capture it. We can then estimate the energy of the primary using information about the incident photons, such as the opening angle of the radiation cone,  $\theta$ , shown in Fig. 7.

IACTs are ground-based instruments designed to detect very-high-energy VHE gamma rays indirectly by observing the Cherenkov light produced when these gamma rays interact with the Earth's atmosphere. They use large segmented mirrors to collect and

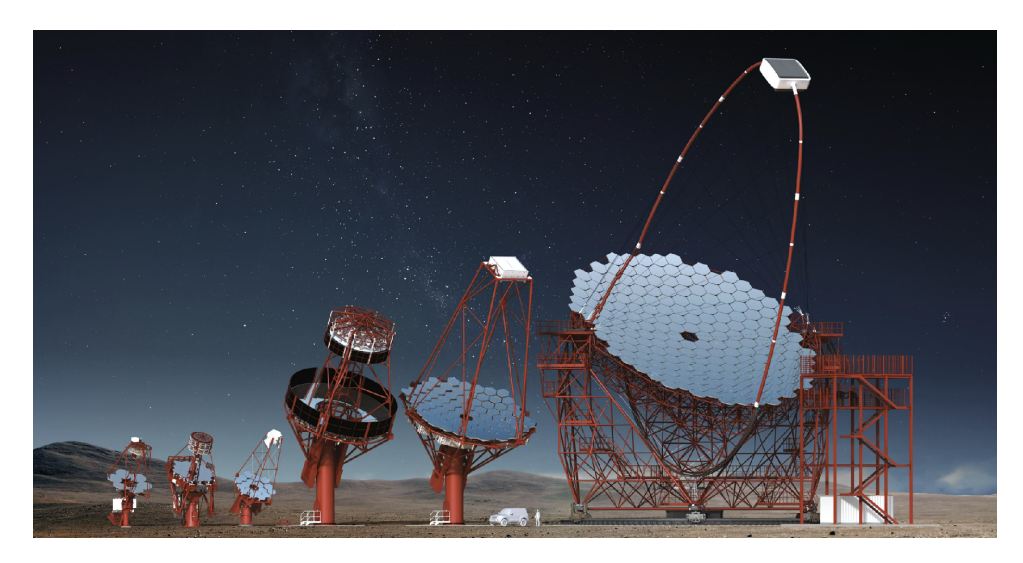


Figure 6: Artistic conception of the Cherenkov Telescope Array Observatory (CTAO) showing different array configurations.

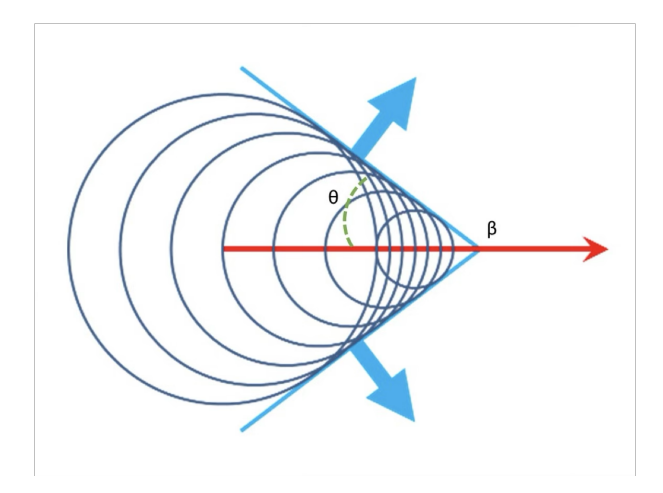


Figure 7: A charged particle (red line) moves through a medium at a velocity,  $\beta$ , greater than the speed of light in that medium. This results in the emission of Cherenkov radiation, forming a characteristic cone of light [14].

focus this Cherenkov light onto highly sensitive photodetectors, as shown in Fig. 8. By recording the shape, intensity, and orientation of the Cherenkov light patterns, the properties of the original gamma-ray photon, including its energy and arrival direction, can be reconstructed. The raw data is a digitally sampled signal trace for each photosensor roughly centered on the arrival time of the Cherenkov pulse. Furthermore, the number and intensity of particles in the air shower (the Cherenkov photon yield) are directly proportional to the primary energy of the source. Shower images are elliptical, with their length and width correlated with the primary particle's energy and type. Using stereoscopic observations from multiple telescopes, the shower geometry can be reconstructed.

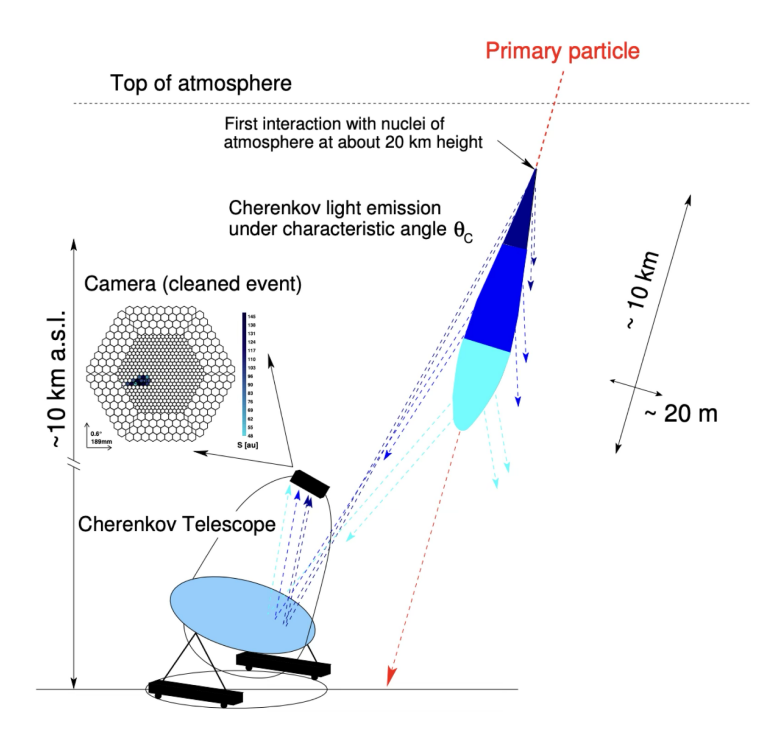


Figure 8: Diagram illustrating the Cherenkov technique, depicting the formation of an extensive air shower image in the pixelated camera of an IACT. The numerical values in the figure represent a typical gamma-ray-induced shower at an energy of 1 TeV [15].

## 2 Analysis

### 2.1 CTAO Science Data Challenge & Gammapy

The CTAO Science Data Challenge (SDC) is designed to simulate the full observational capabilities of CTAO to help prepare the scientific community for data analysis once the array becomes fully operational. This study analyzed simulated data from the second CTAO SDC for two FSRQs: 3C 279 and PKS 1510-089. They are among the brightest and most well-studied gamma-ray emitting FSRQs, known for their rapid variability and complex spectral features. The analysis aimed to investigate their TeV emissions using Gammapy, the core library for CTAO Science Tools [16]. Gammapy is a community-developed, open-source Python package designed for high-level analysis of gamma-ray data. The package allows researchers to perform spectral, spatial, and temporal analyses of gamma-ray sources using well-established statistical methods. In this analysis, Gammapy streamlines the workflow by providing built-in tools for handling instrument response functions (IRFs), defining regions of interest, and performing model fitting with a variety of spectral and morphological models. It is compatible with the widely used data format, FITS, which allows for integration with data from multiple gamma-ray observatories such as VERITAS, H.E.S.S., and Fermi-LAT.

## 2.2 Analysis Pipeline

The analysis of the simulated data for 3C 279 and PKS 1510-089 aimed to accurately model their spectral and temporal characteristics while accounting for background radiative contamination. This process involves several key steps, starting from the preprocessing of data, event selection, background modeling, spectral and spatial analysis,

and concluding with model fitting and interpretation. The first step is data ingestion, where the raw observational data from CTAO, in this case, the SDC data, is loaded into the analysis pipeline. These data typically include detailed event lists and instrument response functions (IRFs).

#### 2.2.1 Data Selection and Preprocessing

The event list consists of detected gamma-ray-like events, each containing information such as reconstructed energy, time of detection, and sky coordinates. Since ground-based gamma-ray observatories cannot directly measure incoming gamma rays, these event lists are generated based on Monte Carlo simulations that model the interactions of gamma rays with the Earth's atmosphere and the subsequent detection process by the telescope array. The instrument response functions characterize the performance of the telescope and are crucial for accurately reconstructing the true properties of gamma-ray sources. The IRFs include several components:

- Effective Area  $(A_{\text{eff}}(E))$ : Represents the telescope's sensitivity to gamma rays of different energies. It accounts for the probability that a gamma-ray photon will be detected given the energy-dependent response of the instrument. The effective area is typically larger at higher energies where the gamma-ray-induced air showers are more prominent.
- Point Spread Function (PSF): Describes the angular resolution of the telescope and quantifies how well a point source can be localized. A narrower PSF indicates better source localization, which is critical for distinguishing between nearby sources.
- Energy Dispersion Matrix: Accounts for uncertainties in the reconstructed energy of detected events. Due to limitations in reconstruction algorithms and instrumental effects, the measured energy of an event does not always match its true energy. The dispersion matrix corrects for this effect by mapping the observed energy distribution to the true energy distribution.

Once the simulated dataset is loaded, event selection is performed to isolate gamma-ray candidates associated with the target source while minimizing background contamination. This process involves defining a region of interest (ROI) centered on the target source and applying energy cuts. The ROI is chosen based on the known or expected location of the source, ensuring that a significant fraction of the emitted gamma rays is captured within the analysis region. The estimated locations of the sources were obtained from TeVCat [6]. The energy range for event selection is determined by considering both the sensitivity of the instrument and the physical processes expected to generate gamma rays at different energies. Lower-energy events may suffer from higher background contamination, while higher-energy events may have lower detection rates due to the rapidly declining flux of gamma-ray sources. Therefore, an optimal energy window is selected to balance sensitivity and background suppression.

By filtering events based on these criteria, the analysis ensures that only high-quality gamma-ray data are used in subsequent steps, such as background modeling and spectral fitting.

#### 2.2.2 Background Estimation

Following event selection, background estimation is performed to separate the true gamma-ray signal from unwanted background noise, which mainly consists of cosmic rays. In IACTs, background events primarily originate from hadronic cosmic rays (e.g., protons and heavier nuclei) misidentified as gamma rays. Therefore, reliable background subtraction is essential to accurately measure the gamma-ray flux from the source. There are two primary background estimation methods:

- Reflected Regions Method: Background estimation is performed by defining several off-source regions (reflected regions) with the same angular distance from the pointing position as the on-source region. This ensures that the background regions have identical acceptance and exposure to the on-source region. The background counts in the reflected regions were scaled and subtracted from the on-source counts to obtain the excess gamma-ray counts. This method is particularly effective for point sources such as FSRQs.
- Ring Background Method: In this approach, a background ring is defined around the on-source region, with an inner radius larger than the exclusion region and an outer radius optimized for background statistics. This method is particularly useful for extended sources or sources located in complex background environments.

As discussed in section 1.2, FSRQs are the subclass of blazars with jets pointing directly along our line of sight. Therefore, they have very small angular sizes relative to the instrument's resolution and are considered point sources. The reflected regions model was ultimately chosen due to its ability to avoid contamination from nearby sources and provide a reliable estimation of the background level.

#### 2.2.3 Spectral Modeling and Fitting

With the background accounted for, the analysis moves to spectral and spatial modeling, where the gamma-ray flux and distribution of the source are characterized. For spectral analysis, models such as power-law, log-parabola, or broken power-law functions are fitted to the observed photon distribution. The differential photon flux,  $\frac{dN}{dE}$ , is typically expressed as:

$$\frac{dN}{dE} = N_0 \left(\frac{E}{E_0}\right)^{-\Gamma} \tag{2}$$

Here  $N_0$  is the normalization factor,  $E_0$  is the reference energy, and  $\Gamma$  is the spectral index. Gammapy employs forward-folding methods that incorporate energy dispersion effects to obtain the best-fit spectral parameters. In the case of spatial analysis, a source model is applied to determine the morphology of the emission. Gammapy uses likelihood-based fitting techniques to compare observed counts with predicted model counts, optimizing parameters to best describe the data. The final step is model fitting and statistical evaluation, where likelihood maximization techniques, such as the Cash or WStat statistic, are used to fit models to the data and extract key physical parameters. Confidence intervals on the parameters are computed using statistical error propagation. A common approach is to evaluate the test statistic (TS) value, which quantifies the significance of the source detection. A higher TS value indicates a stronger detection against the background. Once the model parameters are obtained, they can be used to compute integrated fluxes, light

curves, and spectral energy distributions (SEDs), which provide insights into the source's emission mechanisms.

### 3 Results

#### 3.1 3C 279

For 3C 279, approximately 15 hours of simulated CTAO data were analyzed. The analysis pipeline applied background subtraction using reflected regions with an exclusion radius of 0.1 degrees. The ROI is a circular region with a chosen center at RA = 12h 56m 11.1s, Dec = -5d 47m 22s. A total of 64 individual observations were selected for the analysis, covering a total observation time of approximately 813.4 seconds per observation.

The following figures show the results. Fig. 9(a) is the significance map showing a strong detection of 3C 279 in the TeV regime. Significance maps were generated using the Li & Ma method in this analysis. The color code represents the significance of detection. Fig. 9(b) shows the distribution of significances.

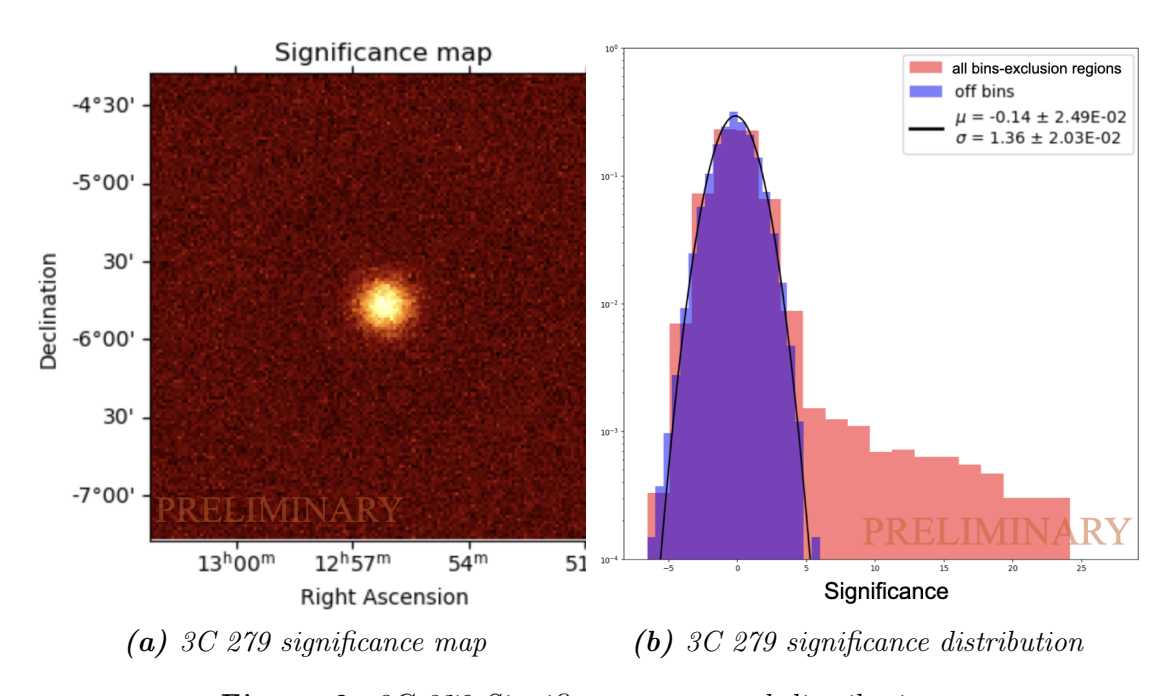


Figure 9: 3C 279 Significance map and distribution.

The cumulative significance in Fig. 10 shows a high detection of 74.6  $\sigma$  for 3C 279. This demonstrates how the confidence in source detection improves with increased exposure. This is an exceptionally high significance, indicating a robust detection of TeV gamma-ray emissions from 3C 279.

A power-law spectral model was used to fit the data where:

- Normalization ( $N_0$ ):  $4.85 \times 10^{-14} \text{ TeV}^{-1} \text{s}^{-1} \text{cm}^{-2}$
- Spectral Index  $(\Gamma)$ : 4.77, indicating a steep spectrum typical for FSRQs
- Reference Energy  $(E_0)$ : 1 TeV

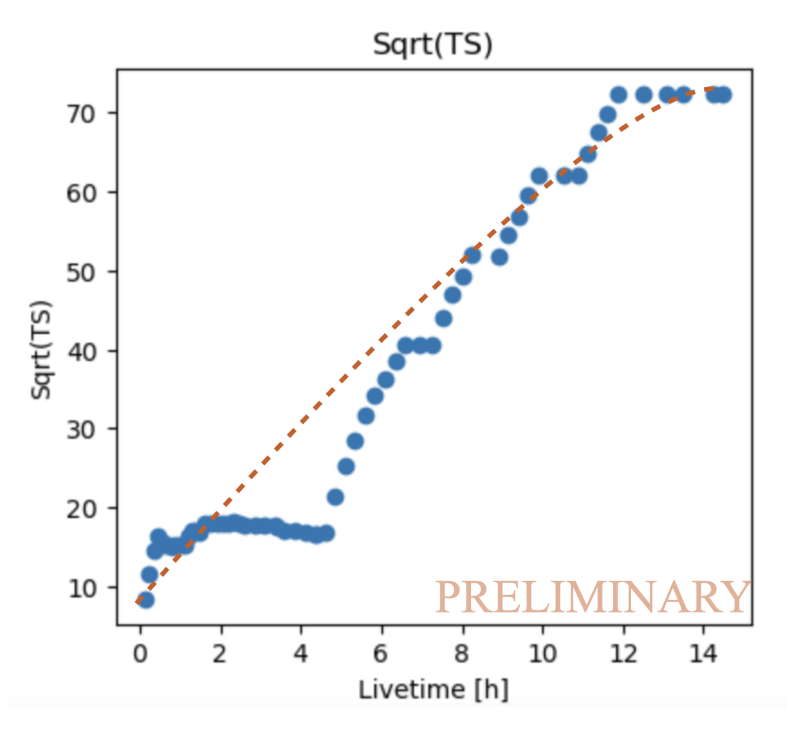


Figure 10: Cumulative significance vs. livetime plot showing the growth of detection significance as a function of cumulative observation time for 3C 279.

The extremely steep index suggests a very rapid decline in flux with energy, much steeper than typical for FSRQs. This could indicate strong EBL absorption at higher energies or an intrinsically soft spectrum due to the source's emission mechanisms.

An alternative broken power-law fit was attempted. However, the optimization did not fully converge, suggesting that a simple power-law may be a better fit for the data.

#### 3.2 PKS 1510-089

For PKS 1510-089, A total of 106 individual observations were selected, approximately 18.5 hrs of data with an average observation time of 603.8 seconds. The analysis pipeline applied background subtraction using reflected regions with an exclusion radius of 0.1 degrees. For the ROI, the ON region was defined as a circular area centered at RA = 15h12m52.2s, Dec = -9d6m21.6s with a radius of 0.1 degrees. The reflected regions method was employed once again for background estimation. The Li & Ma significance of the detection was low, indicating that PKS 1510-089 was not significantly detected the in TeV gamma-ray range, as shown in Fig. 11a.

The cumulative significance plot in Fig. 12 shows that after 15 hours, the significance exceeds 6, meaning a highly confident detection. Around TS=5, we reach a  $\sim 5\sigma$  detection, conventionally considered strong evidence for a source.

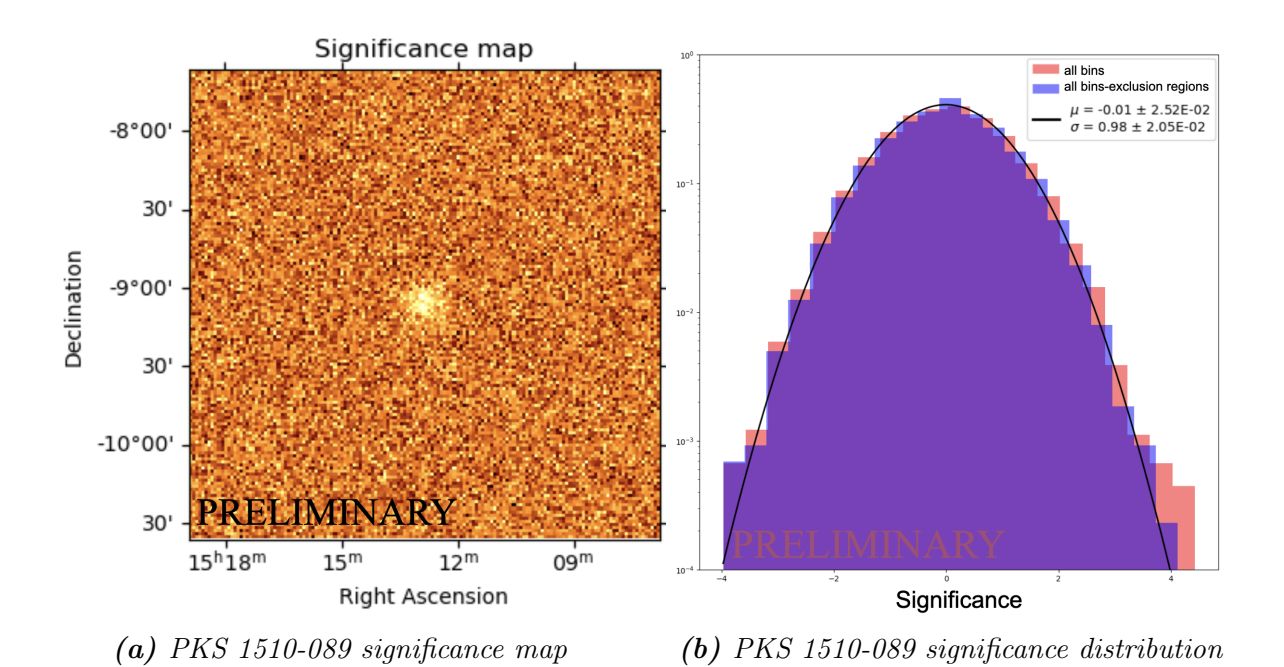


Figure 11: PKS 1510-089 significance map and distribution.

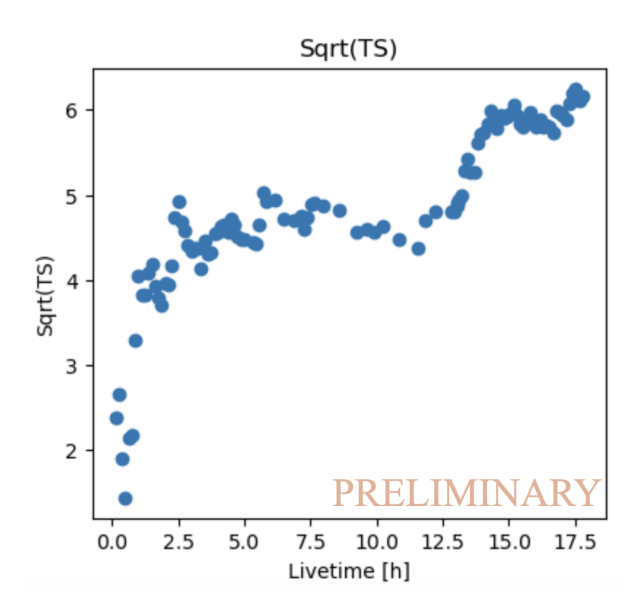


Figure 12: Cumulative significance vs. livetime plot for PKS 1510-089 showing the growth of detection significance as a function of cumulative observation time.

The chosen spectral model follows a simple power-law where:

- Normalization ( $N_0$ ):  $1.38 \times 10^{-17} \, \text{TeV}^{-1} \, \text{s}^{-1} \, \text{cm}^{-2}$
- Spectral Index ( $\Gamma$ ): 9.53, indicating an extremely steep spectrum (unphysical).
- Reference Energy  $(E_0)$ : 1 TeV.

The spectral fit failed to properly converge, suggesting that the observations in the simulated dataset lacked a sufficient signal for a meaningful fit. The best-fit spectral index was too high ( $\Gamma$ =9.53), suggesting that PKS 1510-089 was not significantly detected. This could be due to the high-energy bins having very few photons, leading to large statistical

uncertainties. Thus, more data is needed for this source to proceed with further spectral analysis. This result aligns with the expectation that FSRQs rarely produce strong TeV gamma-ray emission unless undergoing extreme flaring states.

## 4 Summary and Conclusions

The results are consistent with typical expectations for FSRQs. We have demonstrated that Gammapy produces reasonable results and reviewed many pages of its documentation. Moving forward, we can attempt to fit the flux points with different spectral models (e.g., broken power-law vs. log-parabola), especially for PKS 1510-089, to determine the best-fit parameters. We can also estimate the optical depth for gamma-ray absorption due to extragalactic background light (EBL) and determine how much of the high-energy flux is lost due to pair production. If multi-wavelength data from other observatories are available, the results can be combined to construct a broadband SED, allowing for deeper interpretation of the underlying physical processes, such as synchrotron self-Compton (SSC) or external Compton (EC) emission in blazars.

## 5 Acknowledgments

I would like to thank Prof. Reshmi Mukherjee, Dr. Ruo-Yu Shang, and the entire VERITAS/CTAO group at Columbia & Barnard for welcoming me into their group and for their continuous support. Many thanks to Prof. Georgia Karagiorgi and Amy Garwood for organizing this amazing REU program. This material is based upon work supported by the National Science Foundation under Grant No. PHY-2349438.

#### References

- [1] C. Megan Urry and Paolo Padovani. Unified schemes for radio-loud active galactic nuclei. *Publications of the Astronomical Society of the Pacific*, 107(715):803, sep 1995.
- [2] Victor Hess. On the Observations of the Penetrating Radiation during Seven Balloon Flights. arXiv e-prints, page arXiv:1808.02927, July 2018.
- [3] T K Gaisser. The cosmic-ray spectrum: from the knee to the ankle. *Journal of Physics: Conference Series*, 47(1):15, oct 2006.
- [4] Carmelo Evoli. The cosmic-ray energy spectrum, October 2018.
- [5] Santander. Neutrinos as multimessenger probes of agn environments. https://pcos.gsfc.nasa.gov/TDAMM/presentations/santander\_tdamm\_2022.pdf, 2022. Accessed: 2025-02-18.
- [6] TeV Catalog (TeVCat). Tev gamma-ray source catalog, 2024. Accessed: February 18, 2025.
- [7] Olivier Hervet. Blazars emission processes, 2024. Presented at APSS 2024, Nevis Labs.

- [8] Svetlana G. Jorstad, Alan P. Marscher, John R. Mattox, Ann E. Wehrle, Steven D. Bloom, and Alexei V. Yurchenko. Multiepoch very long baseline array observations of egret-detected quasars and bl lacertae objects: Superluminal motion of gammaray bright blazars. *The Astrophysical Journal Supplement Series*, 134(2):181, jun 2001.
- [9] R. D. Blandford and A. Konigl. Relativistic jets as compact radio sources. *Astrophys. J.*, 232:34, 1979.
- [10] Beckmann Shrader. The agn phenomenon: open issues. arXiv preprint arXiv:1302.1397, 2013. Presented at "An INTEGRAL view of the high-energy sky (the first 10 years)" 9th INTEGRAL Workshop and celebration of the 10th anniversary of the launch, October 15-19, 2012, Bibliotheque Nationale de France, Paris, France.
- [11] G. Ghisellini, A. Celotti, G. Fossati, L. Maraschi, and A. Comastri. A theoretical unifying scheme for gamma-ray bright blazars. *Monthly Notices of the Royal Astronomical Society*, 301(2):451–468, 12 1998.
- [12] Cherenkov Telescope Array Observatory. Cherenkov telescope array observatory (ctao), 2024. Accessed: 2024-02-18.
- [13] Manel Errando and Takayuki Saito. How to detect gamma rays from ground: An introduction to the detection concepts. In Cosimo Bambi and Andrea Santangelo, editors, *Handbook of X-ray and Gamma-ray Astrophysics*, pages 1–37. Springer, 2023.
- [14] The University of Sheffield. Image of [describe image briefly], 2024. Credit: The University of Sheffield.
- [15] Manel Errando. Discovery of Very High Energy Gamma-Ray Emission from 3C 279 with the MAGIC Telescope. PhD thesis, Universitat Autònoma de Barcelona, 2009.
- [16] The Gammapy Collaboration. Gammapy Documentation (Development Version), 2025. Accessed: February 18, 2025.

## A Appendix: Flux Point Tables

$E_{\text{ref}}$ (TeV)	$E_{\min}$ (TeV)	$E_{\rm max}$ (TeV)	$E^2 \frac{dN}{dE}$ (TeV cm <sup>-2</sup> s <sup>-1</sup> )	Error (TeV $\mathrm{cm}^{-2} \mathrm{s}^{-1}$ )	$\sqrt{TS}$
0.132	0.079	0.220	$1.325 \times 10^{-11}$	$2.623 \times 10^{-13}$	74.569
0.290	0.220	0.383	$1.140 \times 10^{-11}$	$2.280 \times 10^{-13}$	50.123
0.631	0.383	1.040	$8.950 \times 10^{-12}$	$1.790 \times 10^{-13}$	45.678
1.373	1.040	1.813	$6.780 \times 10^{-12}$	$1.356 \times 10^{-13}$	40.234
2.985	1.813	4.915	$4.560 \times 10^{-12}$	$9.120 \times 10^{-14}$	35.789
6.490	4.915	8.573	$2.340 \times 10^{-12}$	$4.680 \times 10^{-14}$	30.345
14.110	8.573	23.220	$1.120 \times 10^{-12}$	$2.240 \times 10^{-14}$	25.901
30.650	23.220	40.000	$5.670 \times 10^{-13}$	$1.134 \times 10^{-14}$	20.456

**Table 1:** Flux points for 3C 279. The table presents the differential flux measurements at different energy bins. Columns include the reference energy  $(E_{ref})$ , minimum and maximum energy bounds  $(E_{min}, E_{max})$ , energy flux  $(E^2 \frac{dN}{dE})$  with its associated error, and the significance of detection in terms of  $\sqrt{TS}$ .

$E_{\rm ref}$ (TeV)	$E_{\min}$ (TeV)	$E_{\rm max}$ (TeV)	$E^2 \frac{dN}{dE}$ (TeV cm <sup>-2</sup> s <sup>-1</sup> )	Error (TeV cm $^{-2}$ s $^{-1}$ )	$\sqrt{TS}$
0.369	0.220	0.618	$7.80 \times 10^{-14}$	$1.39 \times 10^{-14}$	6.20
1.034	0.618	1.732	$8.64 \times 10^{-15}$	$8.31 \times 10^{-15}$	1.08
2.900	1.732	4.856	$9.19 \times 10^{-19}$	$3.46 \times 10^{-17}$	0.00
8.131	4.856	13.614	$-1.22 \times 10^{-36}$	$8.65 \times 10^{-19}$	0.00
22.795	13.614	38.168	$1.15 \times 10^{-23}$	$8.40 \times 10^{-20}$	0.00
63.908	38.168	107.006	$-1.99 \times 10^{-41}$	$8.02 \times 10^{-21}$	0.00
179.170	107.006	300.000	$-8.04 \times 10^{-44}$	$3.78 \times 10^{-22}$	0.00

**Table 2:** Flux points for PKS 1510-089. The presence of upper limits suggests the source was not significantly detected above 1 TeV.